



Open Archive TOULOUSE Archive Ouverte (OATAO)

OATAO is an open access repository that collects the work of Toulouse researchers and makes it freely available over the web where possible.

This is an author-deposited version published in : <http://oatao.univ-toulouse.fr/>
Eprints ID : 17744

To link to this article : DOI:10.1002/admi.201601185

URL : <http://dx.doi.org/10.1002/admi.201601185>

To cite this version : Aviziotis, Ioannis G. and Duguet, Thomas and Vahlas, Constantin and Boudouvis, Andreas G. *Combined Macro/Nanoscale Investigation of the Chemical Vapor Deposition of Fe from Fe(CO)₅*. (2017) *Advanced Materials Interfaces*. pp. 1601185. ISSN 2196-7350

Any correspondence concerning this service should be sent to the repository administrator: staff-oatao@listes-diff.inp-toulouse.fr

Combined Macro/Nanoscale Investigation of the Chemical Vapor Deposition of Fe from Fe(CO)₅

Ioannis G. Aviziotis, Thomas Duguet, Constantin Vahlas, and Andreas G. Boudouvis*

Experiments and computations are performed to model the chemical vapor deposition of iron (Fe) from iron pentacarbonyl (Fe(CO)₅). The behavior of the deposition rate is investigated as a function of temperature, in the range 130–250 °C, and pressure in the range 10–40 Torr. Furthermore, the evolution of the surface roughness is correlated with the deposition temperature. By combining previously published mechanisms for the decomposition of Fe(CO)₅, a predictive 3D macroscale model of the process is built. Additionally, a nanoscale and a multiscale framework are developed for linking the evolution of the surface of the film with the operating conditions at the reactor scale. The theoretical predictions from the coupled macro/nanoscale models are in very good agreement with experimental measurements indicating poisoning of the surface from carbon monoxide and decrease of the film roughness when temperature increases.

1. Introduction

Iron (Fe) thin films and coatings are involved in a wide spectrum of advanced applications, for example, for the stabilization of magnetic skyrmions in spintronics technology to produce topologically protected spin textures and electronic states for the transportation and storage of information.^[1] They can also be applied as components in magnetic metal multilayers^[1] and in metallic alloys, such as NiFe, FeMn, FePt, and NdFeB to provide advanced materials with high quality magnetic properties^[2] or as dopants to form semi-insulating InP layers.^[3] It was shown recently that the bulk Al₁₃Fe₄ intermetallic alloy presents excellent catalytic activity which may be further improved if processed in the form of thin films.^[4] Several methods have been developed for the production of Fe and Fe-containing thin films, among which chemical vapor deposition (CVD) that combines high deposition rates, moderate process temperatures, reduced effluents volume, and conformal coverage of complex surfaces.

Various Fe metalorganic precursors have been studied for the CVD of Fe films.^[5] More recently, traditional^[6] and new^[7] iron

molecular compounds have been tested for the deposition of iron compounds containing metalloid and nonmetal elements. It thus appears that the design of precursors for the CVD of pure or alloyed Fe films showed limited progress in recent years. This is in part due to the availability of appropriate precursors for pure Fe deposition, such as the widely used iron pentacarbonyl, Fe(CO)₅. Fe(CO)₅ is highly toxic, flammable, and heat-, air-, and light-sensitive. On the other hand, it is a low cost chemical, its transport into the reactor chamber is facilitated by a high vapor pressure at room temperature,^[8] while its low deposition temperature allows the surface treatment of thermally sensitive substrates. Last but not least, despite the

existence of Fe–C bonds, Fe(CO)₅ yields fairly pure Fe films at relatively high deposition rates.^[9] For these reasons, it is reasonable to consider the CVD of Fe from Fe(CO)₅ and consequently it is necessary to establish a robust model which allows process optimization. This is the objective of the present contribution.

The mechanisms of the CVD of Fe from Fe(CO)₅ and the behavior of the latter in CVD conditions have been extensively investigated in the literature. It is proposed that the pentacarbonyl precursor is adsorbed on the surface prior its surface decomposition to Fe and five carbon monoxides (CO).^[10] This global dissociation scheme has also been adopted in other works^[9] where the thermal decomposition of the precursor is studied. However, intermediate surface species such as Fe(CO)₄ and Fe(CO)₃ have been observed experimentally, suggesting that the Fe(CO)₅ surface decomposition involves more than one step.^[11,12]

The CVD of Fe at temperatures higher than 200 °C has also been examined elsewhere.^[8,13] A constant decrease of the Fe deposition rate is observed as temperature increases. This behavior is attributed to the etching of the films by the CO by-product. The same trend for the reduction of the Fe deposition rate above 200 °C has been reported in similar works^[14,15] where it is speculated that besides the effect of CO on growth, homogeneous gas phase reactions of the precursor could also contribute to the decrease of the Fe deposition rate. Finally, it has been shown in a recent study^[16] that CO molecules impact not only the deposition rate but also the microstructure of the Fe films.

The above-mentioned reports do not consider the gas phase whereas it can have a significant effect on the Fe deposition rate. Such information is provided by other authors using infrared spectroscopy^[17] and energy-resolved collision-induced

Dr. I. G. Aviziotis, Prof. A. G. Boudouvis
School of Chemical Engineering
National Technical University of Athens
Heroon Polytechniou 9, 15780 Zografou, Greece

Dr. I. G. Aviziotis, Dr. T. Duguet, Dr. C. Vahlas
CIRIMAT
CNRS

Université de Toulouse
4 allée Emile Monso, BP 44362, 31030 Toulouse cedex 4, France
E-mail: thomas.duguet@ensiacet.fr

dissociation of $\text{Fe}(\text{CO})_5$ and its intermediates^[18] or by computational methods such as ab initio studies.^[19,20] These studies describe the gas phase sequential decarbonylations of the pentacarbonyl precursor and the recombination reactions of the intermediate carbonyls with CO.

The present work provides a combined experimental and theoretical study of the deposition of Fe from $\text{Fe}(\text{CO})_5$. A 3D macroscopic model is developed based on first principles, i.e., the conservation of mass, momentum and energy, and it accounts for transport mechanisms in the bulk of the CVD reactor. In addition, the macroscopic model includes for the first time a detailed chemistry model based on comprehensive literature information, and describes the gas phase and the surface reactions of the precursor. The predictive capability of the model is validated through the comparison of the theoretical output with corresponding experimental results, namely with the deposition rate determined as a function of the deposition temperature.

Microstructural characteristics depend on process conditions, e.g., deposition temperature, operating pressure, and mass inflow rates. In a previous work,^[21] we revealed the effect of the root mean square (RMS), roughness on the electrical

resistivity of Al films. Similarly, it has been proven that surface roughness impacts the magnetoresistance and the magnetic properties of thin films through the increase of the in-plane demagnetization factor^[22] as well as wetting and bio-properties of surfaces.^[23] From this discussion it comes out that the efficient control of film properties passes through a consolidated relation between process parameters and films microstructural characteristics, such as the RMS roughness. This can be met through the nanoscale modeling^[24] and multiscale modeling^[25] of the CVD process. The linking between the two different length scales is performed through the deposition rate which is assumed to remain unchanged regardless the considered scale (see the Supporting Information).^[26]

2. Results and Discussion

2.1. Morphological Observations and Elemental Composition

The microstructures of Fe films deposited at several temperatures between 130 and 250 °C are observed by scanning electron microscopy (SEM) (and presented in **Figure 1**).

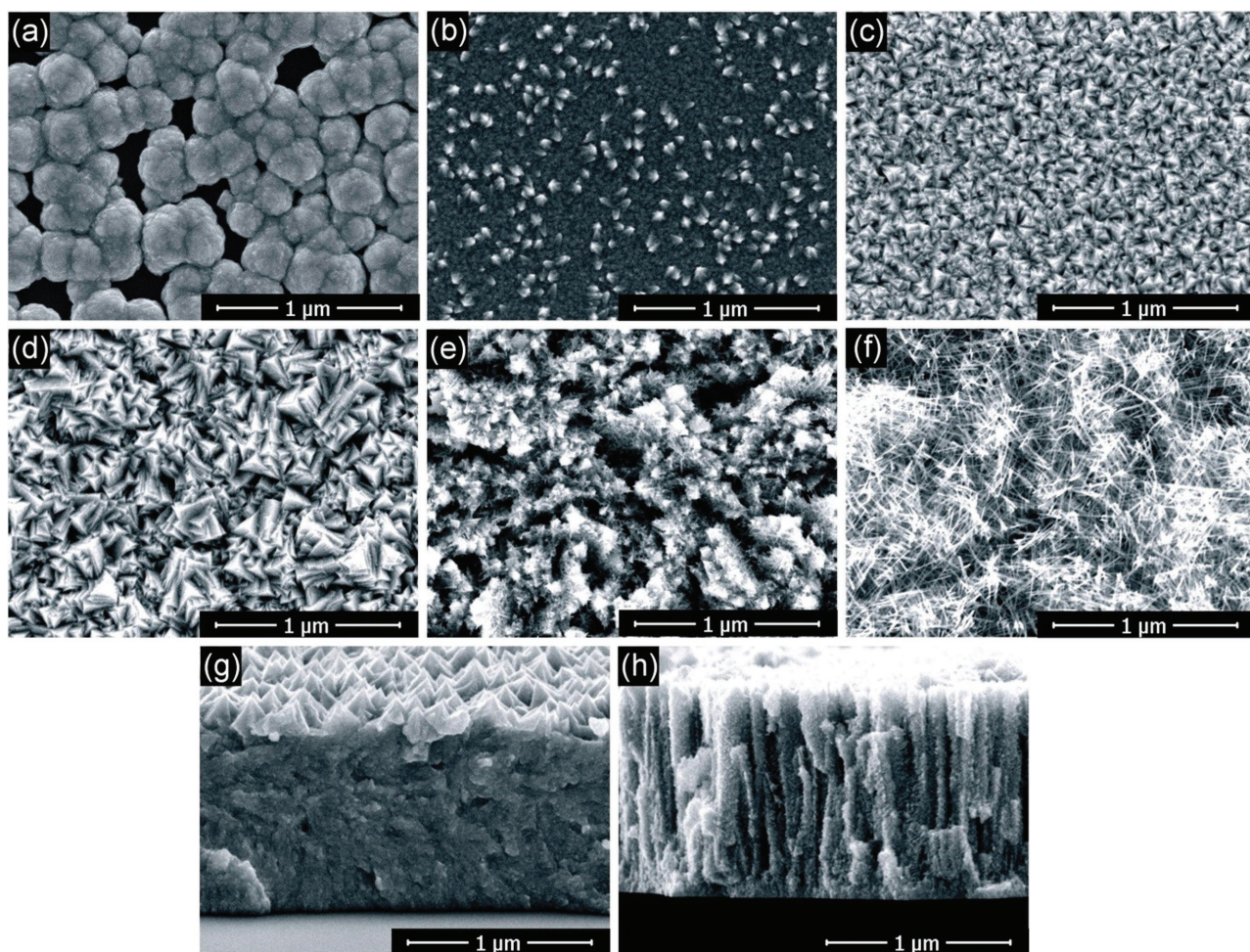


Figure 1. Surface SEM micrographs of Fe films deposited at a) 130, b) 150, c) 170, d) 190, e) 200, and f) 240 °C. Additional cross sections images are shown for g) $T_s = 190$ and h) 200 °C.

Surface micrographs are shown for surface temperatures $130\text{ }^{\circ}\text{C} \leq T_s \leq 240\text{ }^{\circ}\text{C}$ and cross sections are shown for $T_s = 190$ and $200\text{ }^{\circ}\text{C}$. Deposition at the lowest T_s (Figure 1a) shows scattered grains on the surface and yields films with poor uniformity and no continuity. At $T_s = 150\text{ }^{\circ}\text{C}$ (Figure 1b) faceted grains start to form and densify because of grains coalescence. The size of the grains varies, as it is shown in Figure 1b, where some larger grains emerge (bright contrast). When the temperature is increased to 170 and then to $190\text{ }^{\circ}\text{C}$ (Figure 1c,d), angular and sharply faceted grains are formed with apparently homogeneous sizes. The high density of the film and the sharply faceted grain morphology are confirmed from the cross section of Figure 1g. However, at $T_s = 200\text{ }^{\circ}\text{C}$ (Figure 1e) the angular and faceted characteristics of the grains are attenuated. They are gradually replaced by an acicular morphology up to $T_s = 240\text{ }^{\circ}\text{C}$ (Figure 1f). The acicular morphology may result in the increase of porosity, especially for temperatures higher than $200\text{ }^{\circ}\text{C}$. On the other hand, roughness decreases.

The cross section of Figure 1h at $T_s = 200\text{ }^{\circ}\text{C}$, shows a columnar morphology and limited faceting. Whereas films thickness is uniform at the temperature shown in Figure 1g,h, it is relatively poor at lower T_s . Cross sections above $200\text{ }^{\circ}\text{C}$ were not observed, since these temperatures are off-range regarding the co-deposition of Fe with other metals that we target. However, previous works^[16,27] complement our SEM analysis by showing that films deposited above $200\text{ }^{\circ}\text{C}$ or at higher temperatures present a smooth and lamellar morphology.

Measurement of the mass gain, assuming Fe bulk density, gives an estimation of thickness of $3.4 (\pm 0.1\text{ }\mu\text{m})$ and $3.7\text{ }\mu\text{m} (\pm 0.1\text{ }\mu\text{m})$ for 190 and $200\text{ }^{\circ}\text{C}$, respectively, to be compared with SEM measurements of $3.5 (\pm 0.05\text{ }\mu\text{m})$ and $4.0\text{ }\mu\text{m} (\pm 0.05\text{ }\mu\text{m})$, respectively. The comparison of the film thicknesses estimated by mass difference and measured by SEM reveals that the results are similar for the conformal and dense film (Figure 1d) and present small discrepancies for the film of lower density attributed to an increased porosity (Figure 1f).

The composition of the films deposited at $T_s = 160, 200,$ and $240\text{ }^{\circ}\text{C}$ is investigated by electron probe microanalysis (EPMA). At $160\text{ }^{\circ}\text{C}$, Fe is 90% as O and C heteroatoms are up to 4% and 6%, respectively (at%). The C content may be due to the incomplete decomposition of the precursor on the surface at this low T_s and its subsequent incorporation into the film. At $200\text{ }^{\circ}\text{C}$, the Fe and O contents are slightly increased to $\approx 93\%$ and 5.5% , respectively, whereas C is significantly decreased to $\approx 1.5\%$. The increased O contamination can be correlated with the increase of the decomposition rate of the reactants in the gas phase which subsequently leads to O incorporation in the films. The decomposition rate becomes even higher at more elevated temperatures ($240\text{ }^{\circ}\text{C}$) and as a result the O contamination of the film is further increasing to $\approx 9\%$ while Fe and C remain relatively stable (90% – 91% and 1% – 2% , respectively). Similar atomic compositions are also reported by others.^[14] The thermal metalorganic chemical vapor deposition (MOCVD) of Fe from $\text{Fe}(\text{CO})_5$ results in relatively pure films in which the O and C concentrations are a few at%.^[9]

2.2. Dependence of the Fe Deposition Rate on Temperature and Pressure

Figure 2 presents the Arrhenius plot of the process where both experimental measurements and macroscale computational predictions are shown. In the Arrhenius plot the deposition rate continuously increases with increasing T_s up to $180\text{ }^{\circ}\text{C}$, implying a kinetically limited regime. A transition regime is observed in the range 180 – $200\text{ }^{\circ}\text{C}$, where both surface processes and transport phenomena impact the process. In this range, the deposition rate reaches a plateau and a maximum value at $200\text{ }^{\circ}\text{C}$. At higher T_s , competitive phenomena, such as gas phase reactions or diffusion through the mass boundary layer, dominate the process and the deposition rate decreases. The Arrhenius plot is in agreement with previous works^[13] where the deposition rate increases with increasing T_s below $200\text{ }^{\circ}\text{C}$, and remains relatively unaffected above. But more recent studies,^[8,13,14,16] show that beyond $T_s = 200\text{ }^{\circ}\text{C}$ the Fe deposition rate drops in accordance with the present observations. In absolute values, the Fe deposition rate is in agreement with previous results,^[8,13] where a value of 42 nm min^{-1} is obtained at $200\text{ }^{\circ}\text{C}$ as compared to 60 nm min^{-1} at the same temperature in the present work. The same dependence of the deposition rate on the surface temperature is observed in the MOCVD of Ni from $\text{Ni}(\text{CO})_4$,^[8,28] which belongs to the same family of carbonyl precursors.

The computational predictions are in very good agreement with experimental data and the model is able to predict the behavior of the deposition rate over the entire temperature range. In particular, in the low temperature regime, the predicted deposition rate approaches very well the corresponding experimental data and lies within deviations. The large

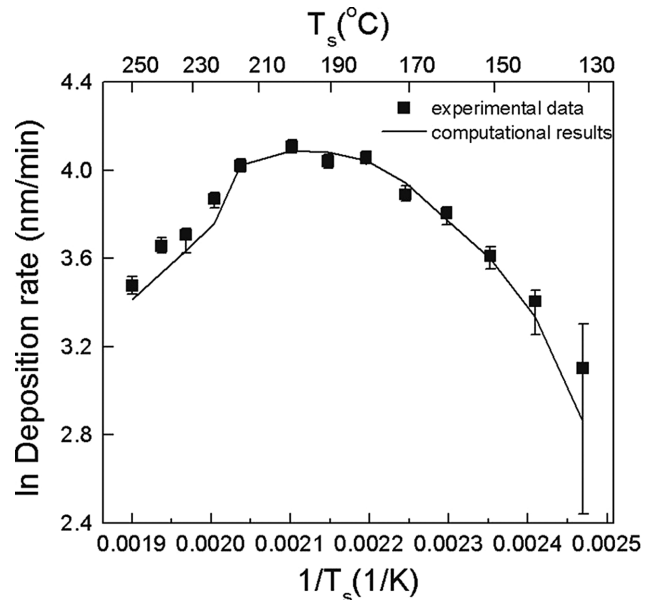


Figure 2. The Arrhenius plot of the CVD of Fe from $\text{Fe}(\text{CO})_5$. The pressure is fixed at $P_{\text{reactor}} = 10$ Torr. Experimental measurements (squares) and computational results (line) are shown. Error bars correspond to the minimum and the maximum deviations of the deposition rate and include potential overestimations of the incubation time.

deviation shown for the lowest T_s experimental point comes from a possible overestimation of the incubation time. As temperature increases, and up to 215 °C, the model continues to predict accurately the measured deposition rates. Above this temperature, the computational model follows the experimental trend that is, a steep reduction with a slight underestimation.

We now further explore the successful prediction of the behavior of the deposition rate. We compare the volumetric reaction rates and the mass fractions of the species which contribute to the deposition rate, in the range 215–223 °C, where the steep reduction of the deposition occurs.

Figure 3 shows the volumetric reaction rates at $T_s = 223$ °C (Figure 3a) and $T_s = 215$ °C (Figure 3b), along a horizontal line 1 mm above the susceptor. Therefore it shows the radial distribution from the center of the susceptor (0 m in the x -abscissa). Reactions which are not shown yield zero reaction rates. At the higher T_s the decomposition rates of the precursor and the tetracarbonyl and tricarbonyl intermediates are higher than the corresponding rates at $T_s = 215$ °C, resulting in the decrease of the precursor available for Fe deposition. Interestingly enough, the rate of recombination of $\text{Fe}(\text{CO})_2$ with CO (green lines) is almost the same as the decomposition rate of $\text{Fe}(\text{CO})_3$ (blue lines). As a result, the $\text{Fe}(\text{CO})_2$ decomposition (Table 1, G4) and consequently the FeCO decomposition (Table 2, SR3) do not occur, since all $\text{Fe}(\text{CO})_2$ intermediates are consumed in the recombination with CO to form $\text{Fe}(\text{CO})_3$. The recombination

of $\text{Fe}(\text{CO})_4$ with CO yields null rates, consistent to literature reports,^[17] whereas the recombination of $\text{Fe}(\text{CO})_3$ with CO occurs at negligible rates ($\approx 10^{-9}$ kmol m^{-3} s^{-1}), due to the consumption of the tricarbonyl by the surface reaction (Table 2, SR2).

Figure 3c shows the mass fractions of $\text{Fe}(\text{CO})_5$ and $\text{Fe}(\text{CO})_3$ at $T_s = 223$ °C (black and red solid lines, respectively) and $T_s = 215$ °C (black and red dashed lines, respectively), still 1 mm above the susceptor. The mass fractions of the other carbonyl species are null. Following the trend of $\text{Fe}(\text{CO})_5$ decarbonylation for these two temperatures, the $\text{Fe}(\text{CO})_5$ available for the surface reaction decreases at $T_s = 223$ °C. On the other hand, $\text{Fe}(\text{CO})_3$ increases with the increased decomposition of $\text{Fe}(\text{CO})_5$. This trend is reinforced in the vicinity of the susceptor where the temperature is higher (see also **Figure 4a,b**, left) and eventually, this combination leads to the decrease of the deposition rate. As shown in Figure 3d, the CO mass fraction is higher at $T_s = 223$ °C contributing to a higher inhibition of the surface processes by CO (Equation (3)) and subsequently to the decrease of the deposition rate. Thus, the model validates the two main reasons for the reduction of the deposition rate at high temperatures that is, increased decomposition rate of the precursor and poisoning of the surface by CO.^[19,21]

Figure 4 shows the temperature (left) and the gas velocity profiles (right) at $T_s = 223$ °C (Figure 4a) and $T_s = 215$ °C (Figure 4b). In both conditions, the temperature increases

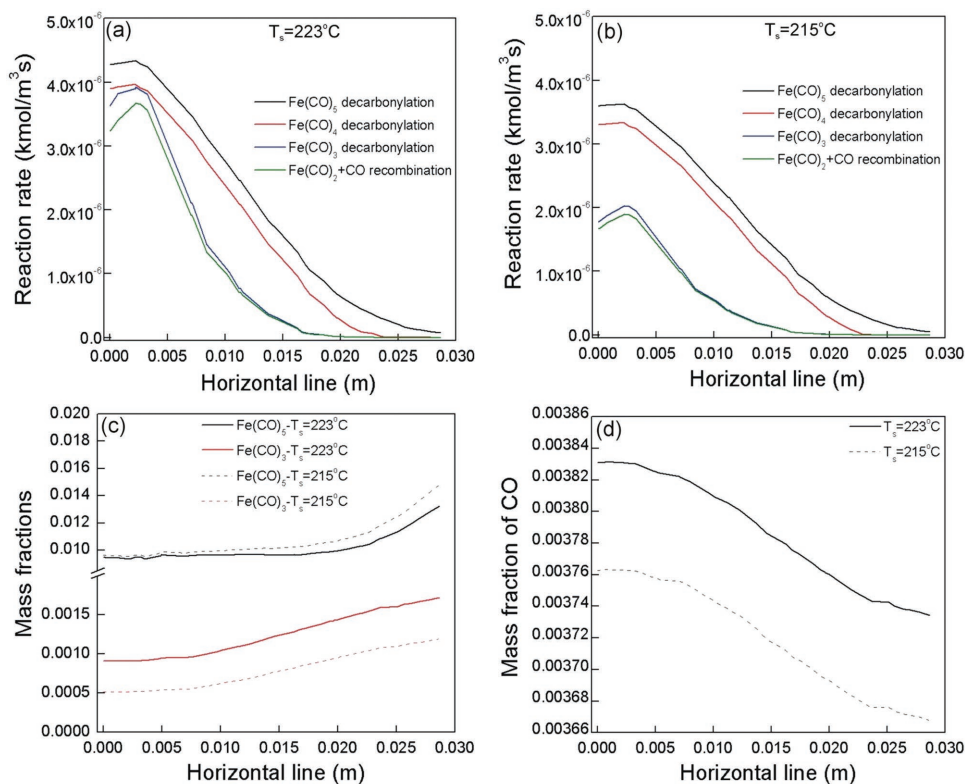


Figure 3. The volumetric reaction rates at T_s a) 223 °C and b) 215 °C. For both figures the black lines correspond to $\text{Fe}(\text{CO})_5$ decarbonylation (Table 1, G1), the red lines to $\text{Fe}(\text{CO})_4$ decarbonylation (Table 1, G2), the blue lines to $\text{Fe}(\text{CO})_3$ decarbonylation (Table 1, G3) and the green lines to $\text{Fe}(\text{CO})_2 + \text{CO}$ recombination (Table 1, G3'). Other reactions give zero rates. c) The mass fractions of $\text{Fe}(\text{CO})_5$ (black lines) and $\text{Fe}(\text{CO})_3$ (red lines) at $T_s = 223$ (solid lines) and 215 °C (dashed lines). d) The mass fraction of CO at $T_s = 223$ (solid line) and 215 °C (dashed line). All the quantities are calculated along a horizontal line 1 mm above the susceptor and are plotted against the radial distribution from the center of the susceptor.

Table 1. The decomposition and the recombination gas phase reactions of $\text{Fe}(\text{CO})_x$, $x = 1 - 5$. The Arrhenius rate expressions are given by Equations (1) and (2).

ID	Reaction	Pre-exponential factor	Activation energy [kJ mol ⁻¹]
G1	$\text{Fe}(\text{CO})_5 \rightarrow \text{Fe}(\text{CO})_4 + \text{CO}$	$9.65 \times 10^{12} \text{ s}^{-1}$	136.7
G2	$\text{Fe}(\text{CO})_4 \rightarrow \text{Fe}(\text{CO})_3 + \text{CO}$	$8.96 \times 10^{12} \text{ s}^{-1}$	79.9
G3	$\text{Fe}(\text{CO})_3 \rightarrow \text{Fe}(\text{CO})_2 + \text{CO}$	$1.25 \times 10^{11} \text{ s}^{-1}$	97.5
G4	$\text{Fe}(\text{CO})_2 \rightarrow \text{FeCO} + \text{CO}$	$3.96 \times 10^{11} \text{ s}^{-1}$	139.1
G1'	$\text{Fe}(\text{CO})_4 + \text{CO} \rightarrow \text{Fe}(\text{CO})_5$	$3.5 \times 10^7 \text{ m}^3 \text{ kmol}^{-1} \text{ s}^{-1}$	10.5
G2'	$\text{Fe}(\text{CO})_3 + \text{CO} \rightarrow \text{Fe}(\text{CO})_4$	$1.3 \times 10^{10} \text{ m}^3 \text{ kmol}^{-1} \text{ s}^{-1}$	9.5
G3'	$\text{Fe}(\text{CO})_2 + \text{CO} \rightarrow \text{Fe}(\text{CO})_3$	$1.8 \times 10^{10} \text{ m}^3 \text{ kmol}^{-1} \text{ s}^{-1}$	9.5

closer to the susceptor and accelerate the gas phase decomposition of $\text{Fe}(\text{CO})_x$ species. In the right panels of Figure 4a,b, it is shown that in both cases the mixture reaches the susceptor with a velocity of 0.5 m s^{-1} and the streamlines reveal that there is a higher concentration at the edges of the susceptor. This fact justifies the elevated concentration of $\text{Fe}(\text{CO})_5$ at this part of the reactor, as observed in Figure 3c as well as the elevated Fe deposition rate (not shown).

We now investigate the effect of the operating pressure, P_{reactor} , on the Fe deposition rate in the range 10–40 Torr at the fixed temperature $T_s = 180 \text{ }^\circ\text{C}$. The results of this investigation are presented in Figure 5a, for both experimental measurements (black squares with black trendline) and computational predictions (cyan triangles with cyan trendline). An eight-fold decrease of the deposition rate from 58 to 7 nm min^{-1} is observed when P_{reactor} is increased from 10 to 40 Torr. A similar trend has been observed in a previous work,^[16] where the increase of the pressure is achieved by adding CO in the input gas mixture and in the case of the CVD of Ni from $\text{Ni}(\text{CO})_4$.^[28] The macroscale computational predictions capture the decrease and the overall behavior of the deposition rate and show very good agreement against the experimental data. In Figure 5b, we present the decomposition rates of $\text{Fe}(\text{CO})_5$ and $\text{Fe}(\text{CO})_3$. The results are shown for $P_{\text{reactor}} = 10 \text{ Torr}$ and $P_{\text{reactor}} = 40 \text{ Torr}$ along a horizontal line located 1 mm above the susceptor. By increasing the pressure the decomposition rates of $\text{Fe}(\text{CO})_5$ and $\text{Fe}(\text{CO})_3$ are increased. This results in the reduction of the deposition rate. Moreover, the increase of P_{reactor} leads to the decrease of the mass diffusion coefficients of these two species

Table 2. The applied surface chemistry model. Reaction rates are given by the Langmuir–Hinshelwood type expression of Equation (3). The pre-exponential factor of reaction SR4 is given in Torr⁻¹, for consistency with the units of Fluent.

ID	Reaction	Pre-exponential factor	Activation energy [kJ mol ⁻¹]
SR1	$\text{Fe}(\text{CO})_5 \rightarrow \text{Fe}_{(s)} + 5\text{CO}_{(g)}$	$2.4 \times 10^7 \text{ m s}^{-1}$	27.9
SR2	$\text{Fe}(\text{CO})_3 \rightarrow \text{Fe}_{(s)} + 3\text{CO}_{(ads)} \rightarrow \text{Fe}_{(s)} + 3\text{CO}_{(g)}$	$5.3 \times 10^7 \text{ m s}^{-1}$	75.3
SR3	$\text{FeCO} \rightarrow \text{Fe}_{(s)} + \text{CO}_{(ads)} \rightarrow \text{Fe}_{(s)} + \text{CO}_{(g)}$	$3.7 \times 10^{10} \text{ m s}^{-1}$	19.3
SR4	CO adsorption	$3.8 \times 10^8 \text{ Torr}^{-1}$	89.9

for an order of magnitude. For these two pressures, the Peclet number, Pe, which provides relative magnitude for diffusion and convection effects, equals $\text{Pe} = 0.95$ at $P_{\text{reactor}} = 10 \text{ Torr}$ and $\text{Pe} = 0.89$ at $P_{\text{reactor}} = 40 \text{ Torr}$. That is, in both pressures $\text{Pe} < 1$ and diffusion phenomena dominate the process. Consequently, the concentration of $\text{Fe}(\text{CO})_5$ and $\text{Fe}(\text{CO})_3$ at the susceptor are lower and the deposition rate is decreased. Thus, the model illustrates that the two main reasons for the reduction of the deposition rate at high pressures are the increased gas phase decomposition rate of the precursor and the decrease of the mass diffusion coefficients of the reactants to the substrate.

2.3. Dependence of RMS Roughness on Temperature

Macroscopic deposition rates are used to fit the s_0 needed in the adsorption rate expression of the stochastic algorithm (Equation (S1), Supporting Information). Figure 6a presents the dependence of the RMS roughness on the temperature for both experimental measurements and computational predictions. We observe that the RMS initially increases up to $150 \text{ }^\circ\text{C}$, from 0.67 to $0.75 \text{ } \mu\text{m}$. Above this temperature and up to $190 \text{ }^\circ\text{C}$, it monotonously decreases from 0.75 to $0.48 \text{ } \mu\text{m}$. The film at $160 \text{ }^\circ\text{C}$ (fourth point from the left) peeled off during the scratching of the surface and for this reason it is probably off the trend. Beyond $200 \text{ }^\circ\text{C}$, the RMS decreases and tends to stabilize at $0.16 \text{ } \mu\text{m}$ in the range 230 – $250 \text{ }^\circ\text{C}$.

The behavior of the RMS roughness is a partial indicator of the change of the microstructure. As shown in Figure 1, at the lowest temperature the coverage of the surface is poor and no faceted crystals are observed. The increase of the deposition temperature up to $150 \text{ }^\circ\text{C}$ results in the enhanced surface coverage and in angular crystals which are sharply faceted. However, the variation of the size of the crystals leads to higher differences between the maximum and the minimum surface heights and to the increase of the RMS. In the temperature range 160 – $190 \text{ }^\circ\text{C}$, the size distribution is more homogeneous, resulting in a monotonous decrease of the roughness. Above $200 \text{ }^\circ\text{C}$ the change of the crystal structure from angular and faceted to acicular results to the sharp decrease of the RMS and then to its stabilization.

It can be seen that the multiscale framework predicts with sufficient accuracy the general behavior of the RMS in the investigated temperature range. However, discrepancies exist at particular T_s . We have seen from the experimental results that at the lowest T_s the coverage of the surface is poor. This feature can lead to an underestimation of the roughness during measurements. Additionally, neglecting the uncovered Si surface in the calculations may cause errors at this temperature. Up to $160 \text{ }^\circ\text{C}$, the model predicts the small changes in RMS quite well, except for the measurement at $130 \text{ }^\circ\text{C}$, where the surface of the film lacks conformal coverage. Moving at higher T_s and until $190 \text{ }^\circ\text{C}$, the experimental RMS decreases and the computational predictions follow this trend. However, the step of abrupt reduction between 190 and $200 \text{ }^\circ\text{C}$ cannot be captured.

As discussed, this reduction is attributed to the change of the crystals morphology from sharp-faceted to acicular. The multiscale model does not simulate the morphology of the crystals accurately and as a consequence, a smoother decrease

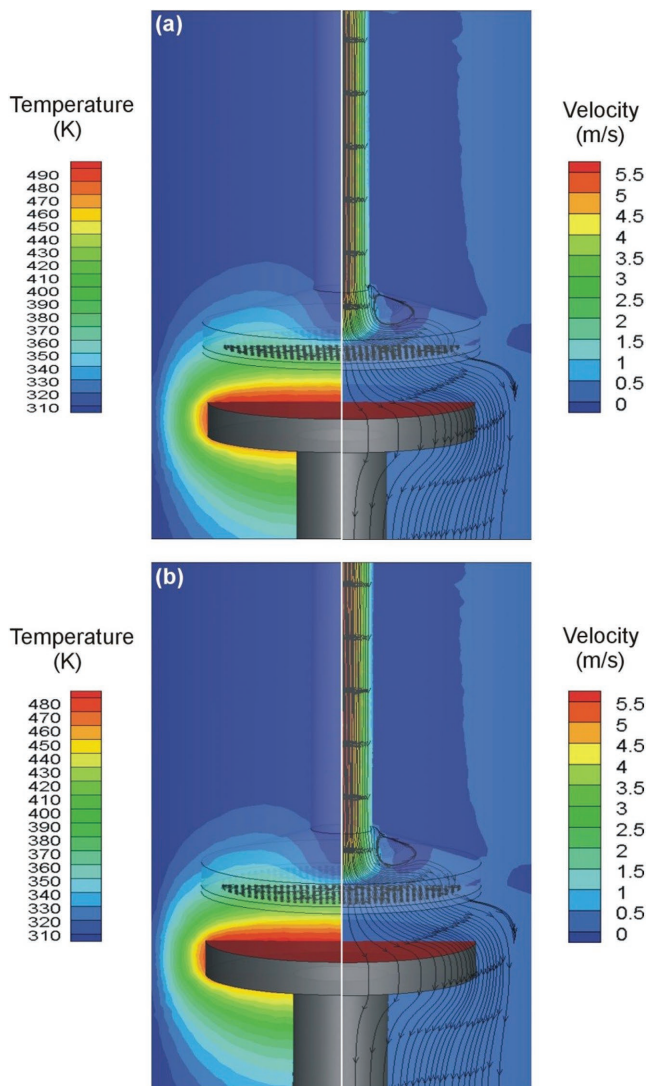


Figure 4. The temperature (left) and the gas velocity (right) profiles inside the reactor during the CVD of Fe from $\text{Fe}(\text{CO})_5$ at T_s a) 223 and b) 215 °C. The streamlines added to the velocity profiles show the flow of the mixture inside the reactor.

of the RMS between these two T_s is predicted. At higher temperatures, it is shown that the computed RMS reaches a plateau; the computational predictions capture well the experimental trend.

We now analyze the occurrence of the kinetic Monte Carlo algorithm events, i.e., adsorption, migration, and desorption. Figure 6b shows the number of surface events—adsorption, desorption, and migration—as a function of T_s . We observe that in the entire temperature range, the number of adsorption events is much higher than the corresponding number of migration and desorption events, and consequently adsorption dominates the process. The trend of adsorption events seems to follow the behavior of the deposition rate (Figure 2) and of s_0 in the investigated temperature range (Equation (S1), Supporting Information), i.e., it increases up to a maximum value at $T_s = 200$ °C, and then it decreases. This is expected since the adsorption rate incorporates s_0 , and it is assumed to

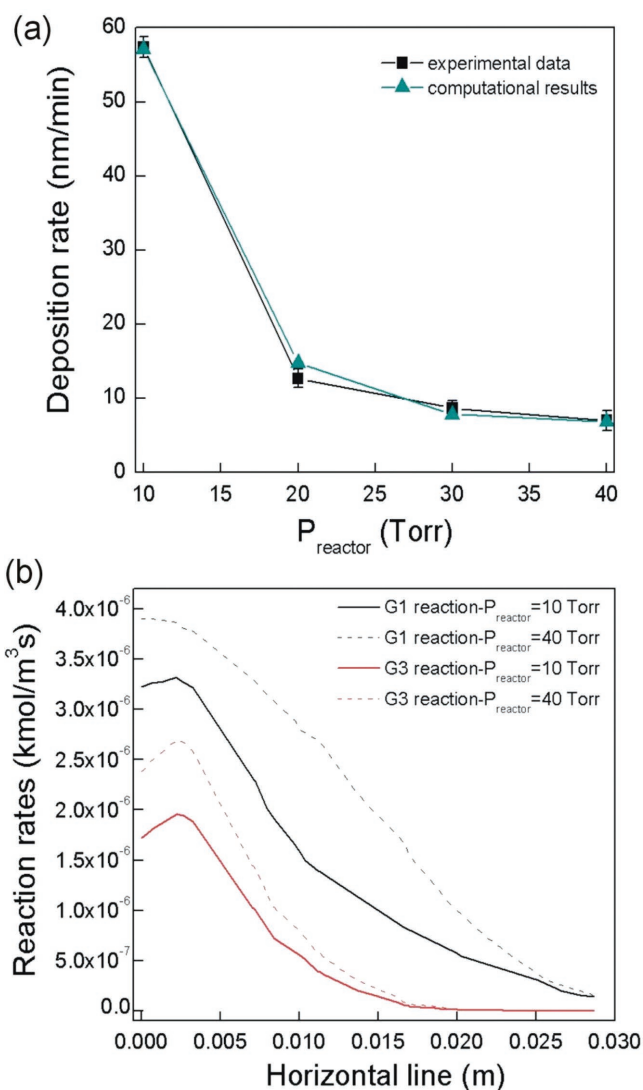


Figure 5. a) The dependence of the deposition rate on P_{reactor} for both experiments (black squares with black trendline) and computational predictions (cyan triangles with cyan trendline). Error bars correspond to the minimum and the maximum deviations of the deposition rate. The temperature is fixed at $T_s = 180$ °C. b) The decomposition rates of G1 (Table 1, black lines) and G3 (Table 1, red lines). All the quantities are calculated along a horizontal line 1 mm above the susceptor and are plotted against the radial distribution from the center of the susceptor.

express the chemical information incorporated in the sticking coefficient. Despite the predominance of adsorption, the impact of the migration, which is not fitted, on the RMS roughness is significant. In particular, it can be seen that as the number of migration events increases, the surface roughness decreases. At higher temperatures in the range 230–250 °C, the number of migration events stabilizes explaining the plateau which is observed for RMS in Figure 6a. The number of desorption events slightly increases up to 200 °C and increases faster up to 250 °C, where they become equal to migration events. It is noted that during the simulations we have observed desorption of Fe atoms with one neighbor, exclusively, in consistence with literature where it is reported that at temperatures up to 250 °C

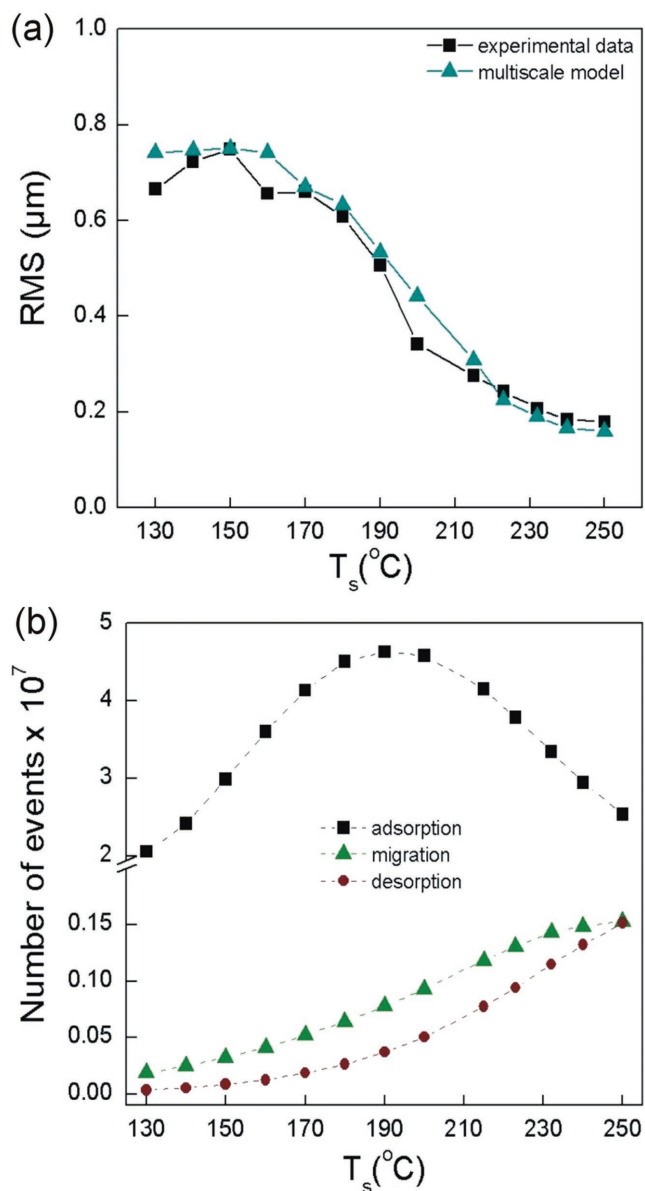


Figure 6. a) Evolution of RMS roughness with surface temperature, T_s . Experimental data (black squares and trendline) and multiscale predictions (cyan triangles and trendline) are shown. b) The number of surface events as a function of T_s . Adsorption, migration, and desorption are illustrated by black squares, green triangles, and brown circles, respectively.

the probability to detach an atom with more than one neighbors is negligible.^[29]

3. Conclusions

The CVD of Fe from $\text{Fe}(\text{CO})_5$ is investigated with the aim to understand and control the behavior of the deposition rate as a function of temperature in the range 130–250 $^{\circ}\text{C}$ and operating pressure at 10–40 Torr. Moreover, the evolution of the roughness is correlated with the deposition temperature within the investigated temperature range.

Deposition results in a relatively pure chemical composition with only a few percent of O and C heteroatoms originating from the precursor. The surface morphology varies with increasing temperature and these variations are correlated with the final surface roughness. In the range 190–200 $^{\circ}\text{C}$, a transition from sharply faceted to acicular morphology is observed which breaks the observed trend.

The Arrhenius plot of the process reveals three regimes. The surface reaction limited regime lies within the temperature range 130–180 $^{\circ}\text{C}$. Between 180 and 200 $^{\circ}\text{C}$, both surface reactions and transport phenomena impact the process. In this range, the Fe deposition rate shows a maximum value of $\approx 60 \text{ nm min}^{-1}$ at 200 $^{\circ}\text{C}$. Beyond this temperature, the process is controlled by the diffusion of the reactants through the mass transport boundary layer to the surface and the deposition rate of Fe decreases abruptly. The macroscopic computational model including the chemistry mechanisms of the process (seven gas phase reactions and three surface reactions) predicts with high accuracy the behavior of the deposition rate in the examined temperature range. It further shows that the steep reduction of the deposition rate at high temperatures is attributed to the high gas phase decomposition rates of the species contributing to the Fe deposition and to the inhibition of the surface from the CO ligand whose surface concentration increases with increasing temperature. Concerning the dependence of the deposition rate on the operating pressure, the combined experimental and computational investigation shows that as pressure increases the gas phase decomposition rates increase and the mass diffusion coefficients of $\text{Fe}(\text{CO})_5$ and $\text{Fe}(\text{CO})_3$ decrease. As a result the concentration of these species at the surface decreases and consequently, the deposition rate decreases.

Following the macroscopic computational analysis, a multiscale framework is developed to simulate the surface of Fe films. The framework predicts the RMS measurements with sufficient accuracy but discrepancies exist. The most important of them lie in the range 190–200 $^{\circ}\text{C}$. In this range, the model shows a monotonous decrease of RMS whereas experimental data show a steep reduction. This discrepancy is attributed to the fact that no information is incorporated in the model concerning the morphology of the crystals and thus, the alteration of the microstructure in this range cannot be predicted. Finally, multiscale simulations at higher temperatures follow the experimental trend, i.e., the stabilization of RMS, in correlation with the number of migration events that reach a plateau.

The developed multiscale computational framework can be implemented to perform simulations for more detailed systems. The incorporation of chemical reactions at the nanoscale and the consideration of the correct crystallographic structure (bcc for Fe) of the developed material within the nanoscale algorithm may allow the simulation of more surface features, such as island or mounts formation during the Fe growth.

4. Macroscopic Model—Chemistry Mechanism

4.1. Gas Phase Reaction and Kinetics

The gas phase scheme consists of successive decarbonylation steps of the pentacarbonyl precursor and recombination of

the free CO ligands with carbonyl intermediates.^[11,12,17–20,30,31] The detailed description of the steps is given in the Supporting Information. The gas phase reactions with their corresponding energies are summarized in Table 1. For this scheme, we modify the Arrhenius law implemented in Fluent to account for the stoichiometry of the reactions. We define two types of Arrhenius reaction rates corresponding to forward (G1–G4) and inverse reactions (G1'–G3'); they are designated by Equations (1) and (2), respectively

$$R_{G_i} = k_{0,G_i} \exp\left(-\frac{E_{a,G_i}}{RT_{\text{gas}}}\right) C_{\text{Fe}(\text{CO})_i,\text{gas}} \quad (1)$$

$$R_{G'_i} = k_{0,G'_i} \exp\left(-\frac{E_{a,G'_i}}{RT_{\text{gas}}}\right) C_{\text{Fe}(\text{CO})_i,\text{gas}} C_{\text{CO},\text{gas}} \quad (2)$$

where R_{G_i} and $R_{G'_i}$ denote the identity of reactions, $C_{\text{Fe}(\text{CO})_i,\text{gas}}$ and $C_{\text{CO},\text{gas}}$ are the gas phase concentrations of each carbonyl species and CO, respectively, E_{a,G_i} and E_{a,G'_i} are the activation energies of the decomposition and the recombination reactions, respectively, and T_{gas} is the temperature of the gas phase in the reactor. The values of the pre-exponential factors of the reverse reactions, k_{0,G'_i} , are obtained from Seder et al.^[17] The pre-exponential factors of the forward reactions, k_{0,G_i} , are fitted to the experimental data. In order to fit the unknown pre-exponential factors of the gas-phase reactions, the process is simulated first at the high-temperature regime, where the gas phase reaction rates are high and gas phase processes becomes dominant for the deposition process. The fitting of these parameters is facilitated by the fact that not all the reactions have the same impact on the behavior of the deposition rate (see Section 2). The pre-exponential factors fitted in the diffusion-limited regime are applied for the simulation of the process in the whole temperature range for a fine tuning. Values of the pre-exponential factors for each reaction are summarized in Table 1.

4.2. Surface Reactions and Kinetics

The surface reaction pathway that we propose combines the works reported in the literature. The $\text{Fe}(\text{CO})_5$ which does not undergo gas phase dissociation, reaches the heated surface and reacts completely for the formation of Fe and five CO groups. For the activation of this reaction, the activation energy of 27.9 kJ mol^{-1} is used, estimated by the slope of the Arrhenius plot in the reaction-limited regime which is in good agreement with the value of $26 \pm 2 \text{ kJ mol}^{-1}$ reported elsewhere.^[9] Then, we consider that the gas phase $\text{Fe}(\text{CO})_3$ which does not decompose, reaches the surface and decomposes to Fe and three CO ligands with an activation energy of 75.3 kJ mol^{-1} .^[11] Finally, the FeCO produced by the successive gas phase decarbonylations of the pentacarbonyl precursor may contribute to the surface deposition of Fe. The activation energy for its bond dissociation equals 19.3 kJ mol^{-1} .^[31] The surface reactions with their corresponding activation energies are summarized in Table 2.

In the above proposed scheme for the surface reactions, we do not consider the exact surface pathway for deposition from

$\text{Fe}(\text{CO})_3$, which includes first, its surface adsorption and then its decomposition to $\text{Fe}(\text{CO})_4$, $\text{Fe}(\text{CO})_3$ and Fe. Instead, we neglect the adsorption of $\text{Fe}(\text{CO})_5$ and we use the gas phase $\text{Fe}(\text{CO})_3$ which reaches the surface, as a source of Fe. In this way, we incorporate its effect on the process and at the same time, we keep the model as simple as possible. It has to be noted that the implementation of a 10-reactions chemistry model (Tables 1 and 2) with their corresponding kinetic rate equations (Equations (1), (2), and (3)) is a complicated task. Thus, we choose to examine first the accuracy of this realistic model with regard to experimental results.

As we briefly discussed in the Introduction, the steep reduction of the deposition rate at high temperatures can be attributed to high gas phase decomposition rate of the precursor and to the poisoning of the surface by CO ligand. Since no adsorption states of the precursor, of its intermediate products or of the CO ligands are incorporated in the model, the effect of CO on the deposition rate can be investigated macroscopically by applying a Langmuir–Hinshelwood type kinetic expression, which is given by the following equation

$$R_{S_i} = \frac{k_{S_i} \exp\left(-\frac{E_{a,S_i}}{RT_s}\right) C_{\text{Fe}(\text{CO})_i,\text{sur}}}{1 + k_{\text{CO}} \exp\left(-\frac{E_{a,\text{CO}}}{RT_s}\right) P_{\text{CO},\text{sur}}} \quad (3)$$

where R_{S_i} is the reaction rate of each surface reaction, $C_{\text{Fe}(\text{CO})_i,\text{sur}}$ is the concentration of the $\text{Fe}(\text{CO})_5$, $\text{Fe}(\text{CO})_3$, and FeCO species at the surface, T_s is the surface temperature, E_{a,S_i} is the activation energy of each surface reaction and k_{S_i} is the pre-exponential factor of the reaction S_i , which is fitted to the experimental data. For the fitting of these parameters, the process is first simulated at the reaction-limited regime where surface reactions are more important than gas phase reactions or diffusion mechanisms. Then, simulations are performed in the whole temperature range for the better fitting of the pre-exponential factors. The denominator of Equation (3), which is referred as SR4 in Table 2, expresses the inhibition of the deposition process by the adsorption of CO. $E_{a,\text{CO}}$ is the adsorption energy of CO which is taken to be 89.9 kJ mol^{-1} ,^[10] $P_{\text{CO},\text{sur}}$ is the partial pressure of CO at the boundary of the surface and k_{CO} is the pre-exponential factor of this process. The latter is fitted to the experimental data as described before, by starting from the diffusion-limited regime, where inhibition by CO is more likely. The values of the pre-exponential factors for each reaction are summarized in Table 2. The implementation of the Langmuir–Hinshelwood expression is performed through user defined functions files.^[32]

5. Experimental Section

Deposition of Fe was performed in a vertical, cylindrical, stagnant flow, cold wall, stainless steel CVD reactor which has been previously described in detail.^[21,33] Independent experiments were performed at 13 different T_s , in the range 130–250 °C for a fixed pressure of $P_{\text{reactor}} = 10 \text{ Torr}$ and at four different P_{reactor} in the range 10–40 Torr, for a fixed $T_s = 180 \text{ °C}$. The deposition duration for all experiments was 1 h, including the incubation time. The incubation time was estimated

by visual observation of the substrate surface through the windows of the reactor and it was only used in the present study to determine the net experimental deposition rate. The rough optical estimation of this parameter might lead to overestimation of the deposition rate, since what it was assumed to be incubation was actually the upper limit of the incubation time. Such overestimations in the measurements of the deposition rate were included in the error bars of the Arrhenius plot (Figure 2).

Samples morphology observations and estimation of the film thickness from cross section images of the film were performed using SEM on a LEO 435 VP microscope running at 15 keV. Surface roughness of Fe films was determined by stylus profilometry (Tencor P16+) across a 1 mm surface line with a lateral resolution of 0.5 μm . EPMA was used to determine the chemical composition of the films and in particular, the O and C content. It was performed with a Cameca SXFive apparatus operating at 15 keV and 20 nA, and calibrated using a high purity Fe standard.

Supporting Information

Supporting Information is available from the Wiley Online Library or from the author.

Acknowledgements

This work was partially funded by the Institut Français du Pétrole et des Énergies Nouvelles (IFPEN) through the contract #268821. I.G.A. acknowledges the financial support provided by the National Scholarship Foundation of Greece (IKY-Siemens Program, Grant number: #SpnD/11160/13 β). The authors acknowledge Ph. De Parseval and L. Mazenq (LAAS) for their help with EPMA and profilometry measurements. The authors are indebted to the European Integrated Center for the Development of New Metallic Alloys and Compounds (C-MAC) for support.

Conflict of Interest

The authors declare no conflict of interest.

Keywords

chemistry mechanisms and kinetics, CVD of Fe, macro/nanoscale modeling, microcilia, roughness simulation

- [1] a) R. Wiesendanger, *Nat. Rev. Mater.* **2016**, *1*, 16044; b) M. N. Baibich, J. M. Broto, A. Fert, F. Nguyen van Dau, F. Petroff, P. Etienne, G. Creuzet, A. Friederich, J. Chazelas, *Phys. Rev. Lett.* **1988**, *61*, 2472.
- [2] a) F. Rottman, F. Dettman, *Sens. Actuators, A* **1991**, *27*, 763; b) B. Diény, V. S. Speriosu, S. Metin, S. S. P. Parkin, B. A. Gurney, P. Baumgart, D. R. Wilhoit, *J. Appl. Phys.* **1991**, *69*, 4774; c) J. P. Liu, Y. Liu, C. P. Luo, Z. S. Shan, D. J. Sellinger, *J. Appl. Phys.* **1997**, *81*, 5644; d) F. J. Cadieu, T. D. Cheung, L. Wickramasekara, N. Kamprath, H. Hegde, N. C. Liu, *J. Appl. Phys.* **1987**, *62*, 3866.
- [3] A. T. Macrander, J. A. Long, V. G. Riggs, A. F. Bloemeke, W. D. Johnston Jr., *Appl. Phys. Lett.* **1984**, *45*, 1297.
- [4] M. Armbrüster, K. Konvir, M. Friedrich, D. Teschner, G. Wowsnick, M. Gahne, P. Gille, L. Szentmiklósi, M. Feuerbacher, M. Heggen, F. Girgsdies, D. Rosenthal, R. Schlögl, Y. Grin, *Nat. Mater.* **2012**, *11*, 690.
- [5] V. Krisyuk, A. N. Gleizes, L. Aloui, A. Turgambaeva, B. Sarapata, N. Prud'homme, F. Senocq, D. Samélor, A. Zielinska-Lipiec, D. de Caro, C. Vahlas, *J. Electrochem. Soc.* **2010**, *157*, D454, and references therein.
- [6] a) N. Pachauri, B. Khodadadi, A. V. Singh, J. B. Mohammadi, R. L. Martens, P. R. LeClair, C. Mewes, T. Mewes, A. Gupta, *J. Magn. Mater.* **2016**, *417*, 137; b) M. Lubej, I. Plazl, *Chem. Eng. J.* **2014**, *242*, 306; c) N. Berry, M. Cheng, C. L. Perkins, M. Limpinsel, J. C. Hemminger, M. Law, *Adv. Energy Mater.* **2012**, *2*, 1124.
- [7] a) S. Mlowe, D. J. Lewis, M. A. Malik, J. Raftery, E. B. Mubofu, P. O'Brien, N. Revaprasadu, *Dalton Trans.* **2016**, *45*, 2647; b) R. A. Hussain, A. Badshah, A. Younis, M. D. Khan, J. Akhtar, *Thin Solid Films* **2014**, *567*, 58; c) G. Fornalczyk, M. Valldor, S. Mathur, *Cryst. Growth Des.* **2014**, *14*, 1811; d) D. Peeters, G. Carraro, C. Maccato, H. Parala, A. Gasparotto, D. Barreca, C. Sada, K. Kartaschew, M. Havenith, D. Rogalla, H.-W. Becker, A. Devi, *Phys. Status Solidi A* **2014**, *211*, 316; e) S. Saeed, R. Hussain, R. J. Butcher, *J. Coord. Chem.* **2014**, *67*, 1693; f) R. Mantovan, S. Vangelista, S. Cocco, A. Lamperti, O. Salicio, *J. Appl. Phys.* **2012**, *111*, 3; g) S. D. Disale, S. S. Garje, *Appl. Organomet. Chem.* **2010**, *24*, 734.
- [8] P. A. Lane, P. J. Wright, P. E. Oliver, C. L. Reeves, A. D. Pitt, J. M. Keen, M. C. Ward, M. E. Tilsley, N. A. Smith, B. Cockayne, I. Rex Harris, *Chem. Vap. Deposition* **1997**, *3*, 97.
- [9] R. B. Jackman, J. S. Foord, *Surf. Sci.* **1989**, *209*, 151.
- [10] H. E. Carlton, J. H. Oxley, *AIChE J.* **1965**, *11*, 79.
- [11] F. Zaera, *Surf. Sci.* **1991**, *255*, 280.
- [12] M. Xu, F. Zaera, *Surf. Sci.* **1994**, *315*, 40.
- [13] P. A. Lane, P. J. Wright, *J. Cryst. Growth* **1997**, *204*, 298.
- [14] F. Senocq, F.-D. Duminica, F. Maury, T. Delsol, C. Vahlas, *J. Electrochem. Soc.* **2006**, *153*, G1025.
- [15] Y. H. Low, J. H. Montgomery, H. S. Gamble, *ECS Trans.* **2007**, *2*, 167.
- [16] P. Zhang, E. Mohimi, T. K. Talukdar, J. R. Abelson, G. S. Girolami, *J. Vac. Sci. Technol. A* **2016**, *34*, 051518.
- [17] T. A. Seder, A. J. Ouderkirk, E. Weitz, *J. Chem. Phys.* **1986**, *85*, 1977.
- [18] L. S. Sunderlin, D. Wang, R. R. Squires, *J. Am. Chem. Soc.* **1992**, *114*, 2788.
- [19] L. A. Barnes, M. Rosi, C. W. Bauschlicher Jr., *J. Chem. Phys.* **1991**, *94*, 2031.
- [20] O. González-Blanco, V. Branchadell, *J. Chem. Phys.* **1999**, *110*, 778.
- [21] a) I. G. Aviziotis, N. Cheimarios, T. Duguet, C. Vahlas, A. G. Boudouvis, *Chem. Eng. Sci.* **2016**, *155*, 449, and references therein; b) I. G. Aviziotis, *Ph.D. Thesis*, National Technical University of Athens, Greece, **2016**.
- [22] G. Choe, M. Steinback, *J. Appl. Phys.* **1999**, *85*, 5777.
- [23] a) E. Bormashenko, T. Stein, G. Whyman, Y. Bormashenko, R. Pogreb, *Langmuir* **2006**, *22*, 9982; b) V. P. Zhdanov, K. Rechendorff, M. B. Hovgaard, F. Besenbacher, *J. Phys. Chem. B* **2008**, *112*, 7267.
- [24] a) C. C. Battaile, D. J. Srolovitz, *Annu. Rev. Mater. Res.* **2002**, *32*, 297; b) C. Cavallotti, A. Barbato, A. Veneroni, *J. Cryst. Growth* **2004**, *206*, 371; c) A. Chatterjee, D. G. Vlachos, *J. Comput.-Aided Mater. Des.* **2007**, *14*, 253; d) D. T. Gillespie, *J. Phys. Chem.* **1977**, *81*, 2340; e) D. T. Gillespie, *J. Chem. Phys.* **2001**, *115*, 1716.
- [25] a) N. Cheimarios, S. Garnelis, G. Kokkoris, A. G. Boudouvis, *J. Nanosci. Nanotechnol.* **2011**, *11*, 8132; b) P. D. Christofides, A. Armaou, Y. Lou, A. Varshney, in *Control Engineering Series* (Ed: W. S. Levine), Birkhäuser, Boston, MA, **2008**; c) Y. Lou, P. D. Christofides, *Chem. Eng. Sci.* **2003**, *58*, 3115; d) S. T. Rodgers, K. F. Jensen, *J. Appl. Phys.* **1998**, *83*, 524.

- [26] M. Masi, V. Bertani, C. Cavallotti, S. Carra, *Mater. Chem. Phys.* **2000**, *66*, 229.
- [27] T. Delsol, F. Maury, F. Senocq, in *Fifteenth European Conference on Chemical Vapor Deposition (EUROCVI-15)*, Proceedings Vol. 2005–09 (Eds: A. Devi, R. Fischer, H. Parala, M. Allendorf, M. Hitchman), The Electrochemical Society Inc., NJ, **2005**, pp. 638–643.
- [28] F. Fau-Canillac, F. Maury, *Surf. Coat. Technol.* **1994**, *64*, 21.
- [29] J. G. Amar, F. Family, *Phys. Rev. Lett.* **1995**, *74*, 2066.
- [30] C. Dateo, T. Gökçen, M. Meyyappan, *J. Nanosci. Nanotechnol.* **2002**, *2*, 523.
- [31] A. Ricca, *Chem. Phys. Lett.* **2001**, *350*, 313.
- [32] Ansys/Fluent v12.1sp1. Documentation. Ansys Inc., **2009**.
- [33] a) T. C. Xenidou, A. G. Boudouvis, N. C. Markatos, D. Samélor, F. Senocq, N. Prud'homme, C. Vahlas, *Surf. Coat. Technol.* **2007**, *201*, 8868; b) T. C. Xenidou, N. Prud'homme, C. Vahlas, N. C. Markatos, A. G. Boudouvis, *J. Electrochem. Soc.* **2010**, *157*, D633.